A Novel Unsymmetrical Coupling Structure Based on Concentrated Magnetic Flux for High-Misalignment IPT Applications

Yousu Yao, *Student Member, IEEE*, Yijie Wang, *Senior Member, IEEE*, Xiaosheng Liu, *Member, IEEE*, Yu Pei, and Dianguo Xu, *Fellow, IEEE*

***Abstract*—The capability of misalignment tolerance is vital for an inductive power transfer system. This paper proposes a novel unsymmetrical coupling structure that can remarkably enhance the output voltage stability with respect to the horizontal, vertical, and angular displacements. The core of this structure is concentrated magnetic field. The optimization method to derive the optimal loosely coupled transformer providing the strongest tolerance to misalignment and fulfilling the requirement of the minimum coupling coefficient is presented. The proposed structure is compared with planar circular and square coils and double-D (DD) coupler from the perspectives of magnetic coupling and anti-misalignment capability. A 200-W prototype is finally fabricated, where the primary series, secondary series-parallel compensation topology is employed to further improve the system's tolerance to misalignment. A maximum output voltage ripple factor of 2.83% and a minimum system efficiency of 91.9% are achieved when the horizontal displacement is as high as one-third of the coupling coil.**

***Index Terms*—Concentrated magnetic field, inductive power transfer (IPT), magnetic design, misalignment tolerance, primary series, secondary series-parallel (S/SP) compensation topology.**

I. Introduction

INDUCTIVE power transfer (IPT) has aroused more and more attention in recent years due to its advantages of low maintenance, high reliability, flexibility, safety, and environmental friendliness [1]. It has been researched for many applications including electric vehicle charging, household appliances, portable electronic devices, autonomous underwater vehicles, satellites, medical implants, etc.

Manuscript received January 10, 2018; revised March 19, 2018 and May 14, 2018; accepted June 22, 2018. Date of publication June 25, 2018; date of current version February 20, 2019. This work was supported in part by the National Natural Science Foundation of China under Grant 51777038, in part by the Fundamental Research Funds for the Central Universities under Grant HIT.BRETIII.201510, in part by the National High Technology Research and Development Program 863 of China under Grant 2015AA050603, in part by the National Natural Science Foundation of China under Grant 51677034, and in part by the Natural Science Foundation of Heilongjiang Province of China under Grant ZD2018012. Recommended for publication by Associate Editor O. C. Onar. *(Corresponding author: Yijie Wang.)*

The authors are with the School of Electrical Engineering and Automation, Harbin Institute of Technology, Harbin 150001, China (e-mail:

3-D orthogonal ferrite coils are relatively large. What is more, the tolerance to horizontal and vertical shifts is not encompassed in [14] and [15]. The ACS proposed by Chun T. Rim and his research partners provide high tolerance to both lateral and longitudinal displacements and air gap variation. The ACS are similar to the DD coil to some extent. However, for ACS, the dimensions of the primary coil are different from those of the secondary one; for DD coil, they are the same. The third type of study endeavors to strengthen the anti-misalignment capability by means of employing variable inductance or variable switched capacitance [17]–[19]. The electrical characteristics of the resonant tank can be altered by employing variable inductance or variable switched capacitance; therefore, the output power can be regulated. The employment of variable inductance results in higher power loss since the ferrite core is sometimes saturable. The authors firmly believe that the misalignment issue can only be solved by comprehensively using the three technologies which have been mentioned above.

The analysis and optimization of an IPT system against misalignment tolerance is very important for performance evaluation and enhancement. Fotopoulou and Flynn built an analytical model of IPT systems, where the effects of coil misalignment and geometry are incorporated [20], [21]. This analytical model makes great sense in the optimization of the coil geometry for highest misalignment tolerance. Sampath *et al.* proposed a figure of merit in [22] in order to obtain an IPT system with high power transfer efficiency (PTE), strong power transfer capability, and excellent misalignment tolerance. Misalignments in six degrees of freedom are analyzed. The performance of the optimized IPT system against misalignment is improved by using the figure of merit.

This paper proposes a novel unsymmetrical coupling structure (UCS) based on the idea of concentrated magnetic flux. The physical appearance and geometry parameters describing the dimension of the structure will initially be introduced. The optimization method to derive the best coupling coil is subsequently elaborated. The comparison with the three existing structures is also incorporated. In order to improve the capability of misalignment tolerance, the S/SP compensation topology is employed. The compensation parameters are deliberately designed. A prototype is fabricated, based on which the verification experiments are carried out. Several findings are summarized in the final section.

II. Proposed UCS

A. Physical Appearance and Geometry Parameters of the Proposed Structure

Fig. 1 shows the schematic view of the proposed UCS captured from ANSYS Maxwell. The shade in gray represents ferrite, while the shade in purple stands for winding. The secondary winding (SW) and ferrite are in the planar square ring form, while the primary winding (PW) and ferrite are in the tridimensional square ring form. The parameters D_{tra}, OSL_S, and H_P, which are labeled in Fig. 1(b), represent the power transfer distance (PTD), the outer side length of the secondary coil, and the height of the primary coil, respectively. For the

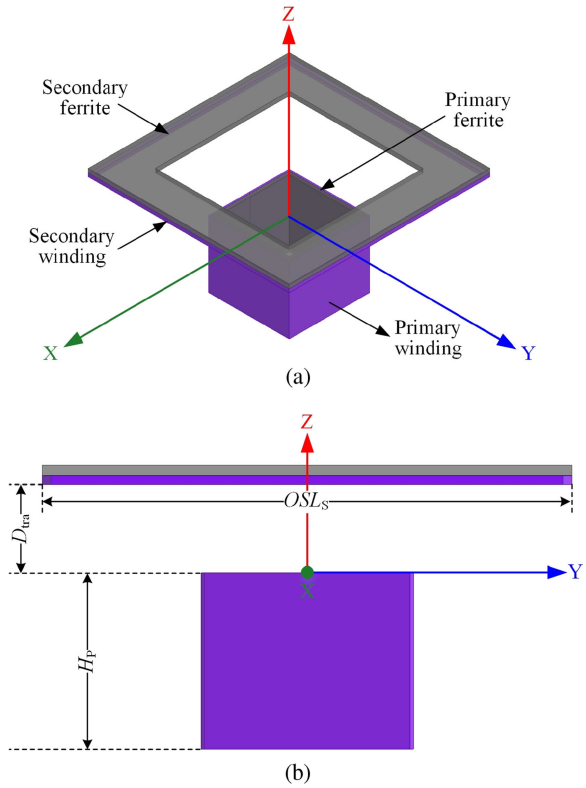

Fig. 1. Schematic view of the proposed UCS. (a) Isometric view. (b) Front view.

sake of clarity, the four components of the proposed UCS are separately shown in Fig. 2. The geometry parameters which determine the dimensions of the coupling structure are labeled in the corresponding diagrams.

The UCS proposed in this paper is different from the ACS proposed in [16]. First, UCS is a transformation of the conventional square coils, whereas ACS is an improvement of the conventional DD coupler. Second, UCS provides identical lateral and longitudinal (*X*-direction and *Y*-direction in Table IV) misalignment tolerance, but ACS offers unequal lateral and longitudinal misalignment tolerance. ACS provides strong lateral misalignment tolerance but poor longitudinal misalignment tolerance. This characteristic limits the utilization of ACS in many applications, such as wireless charging for consumer electronics and kitchen appliances. Third, UCS shows excellent misalignment tolerance to angular displacement. However, ACS exhibits fairly poor capability in resisting angular displacement. This is not vital in some applications, such as electric-vehicle charging. Nevertheless, it is unacceptable in most applications as it results in great inconvenience to the users. Fourth, the mechanical structure of UCS is simpler. As a consequence, the embedding, fixing, and installation of UCS are easier.

B. Concept of Concentrated Magnetic Flux

Fig. 3 shows the two-dimensional (2-D) magnetic flux distribution of the proposed UCS. The plane of Fig. 3(a) is parallel to the *X*–*Y* plane and is located at the center of the primary and secondary coupling coils (see Fig. 1); the areas in red and yel-

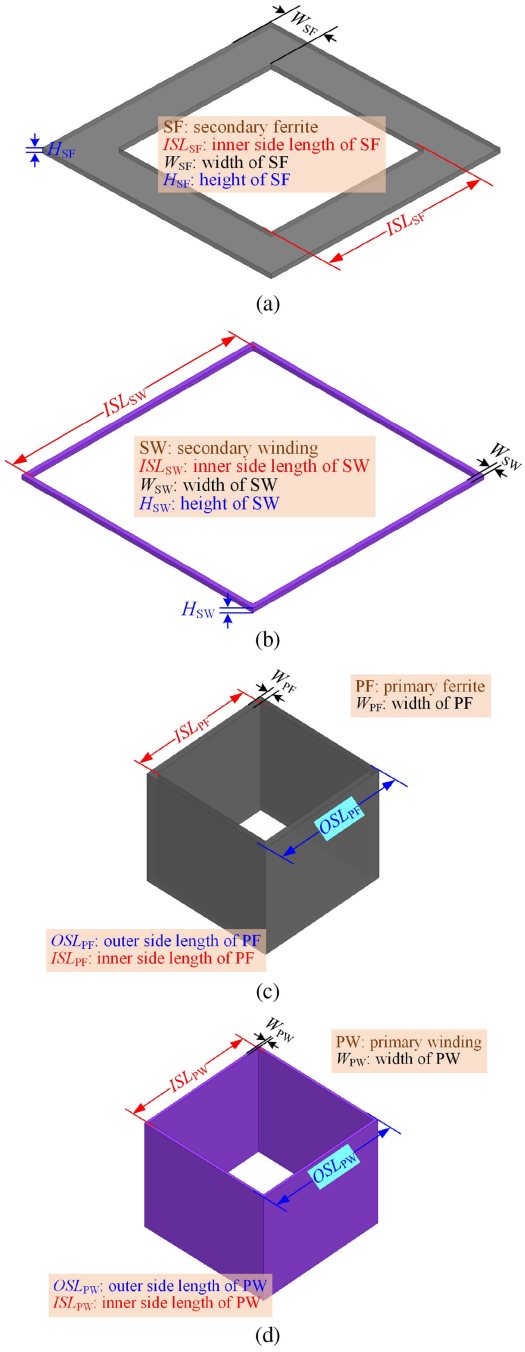

Fig. 2. Separated diagrams of the four components in the proposed UCS. (a) SF. (b) SW. (c) PF. (d) PW.

low, which are mainly situated in the center of the square plane, indicate a stronger magnetic flux. The plane of Fig. 3(b) is the *X*–*Z* plane. Both the primary and secondary coupling coils are symmetrical with respect to the plane. The length of the region with a relatively high magnetic flux intensity ($L_{\text{HMF-pro}}$) is much smaller than 400 mm. The magnetic flux is mainly concentrated in the space around the transmitter pad.

The 2-D magnetic flux distribution of the conventional planar square coupling structure (PSCS) is shown in Fig. 4. Both the primary and secondary couplers of the PSCS are the same as the

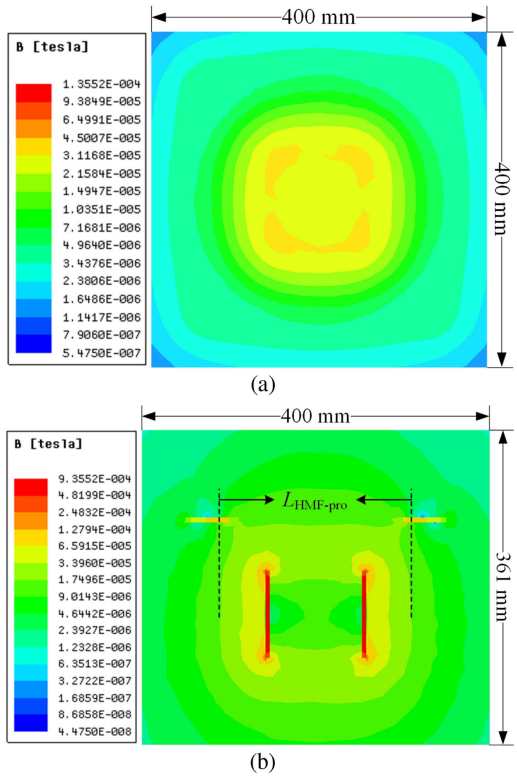

Fig. 3. 2-D flux distribution of the proposed UCS. (a) In the plane that is parallel to *X*–*Y* plane and locates at the center of the primary and secondary coupling coils. (b) *X*–*Z* plane.

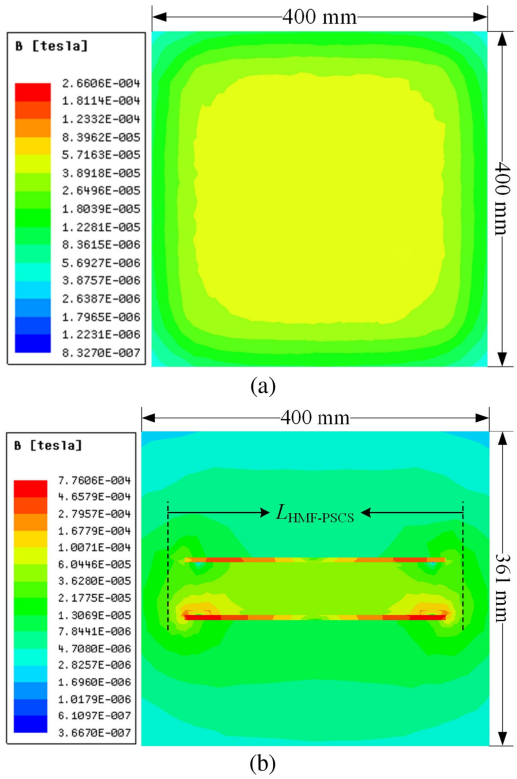

Fig. 4. 2-D magnetic flux distribution of the conventional PSCS. (a) In the plane that is parallel to *X*–*Y* plane and locates at the center of the primary and secondary coupling coils. (b) *X*–*Z* plane.

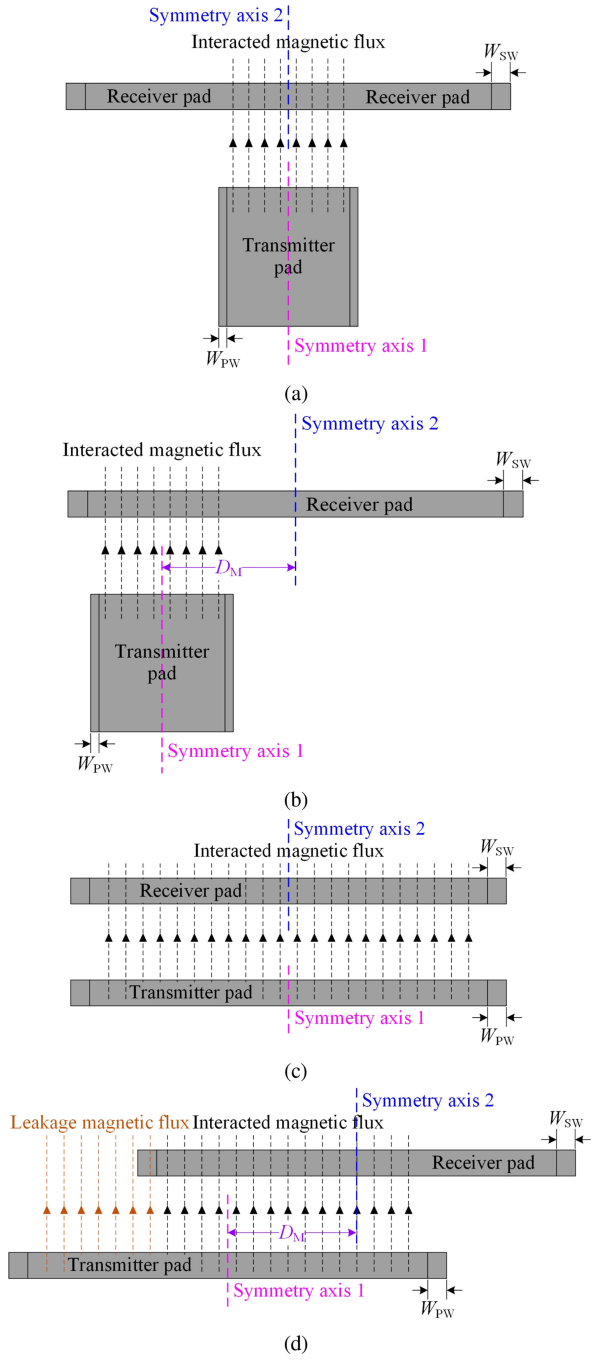

Fig. 5. Magnetic flux diagram of the newly proposed unsymmetrical structure and the conventional planar square structure under aligned and misaligned conditions. (a) Proposed structure in aligned situation. (b) Proposed structure in misaligned situation. (c) Conventional structure in aligned situation. (d) Conventional structure in misaligned situation.

secondary coupler of the proposed structure, but the winding is seated on the ferrite for the primary coupler (see Table IV). The relative orientations between the coupling coils and the magnetic flux distribution planes are the same as those in Fig. 3. Compared to Fig. 3(a), the area exposed to a stronger magnetic flux becomes larger and locates farther from the center of the square plane. This result can also be obtained by comparing Figs. 3(b) and 4(b). Here, $L_{\text{HMF-PSCS}}$ are much bigger than $L_{\text{HMF-pro}}$, indicating a more dispersed magnetic flux.

TABLE I
SPACE CONSTRAINTS OF THE LCT AND PTD

Symbol	Parameter	Value
SL_{pri}	Side length of primary coil	150 mm
H_{pri}	Height of primary coil	100 mm
SL_{sec}	Side length of secondary coil	300 mm
H_{sec}	Height of secondary coil	15 mm
D_{tra}	Power transfer distance	50 mm

In light of the comparison between Figs. 3 and 4, the proposed structure provides a more concentrated magnetic field than PSCS. More concentrated magnetic flux distribution indicates a stronger capability of misalignment tolerance. This can be explained by Fig. 5, where the magnetic flux distribution of the newly proposed unsymmetrical structure and the conventional planar square structure under aligned and misaligned conditions are presented. The magnetic flux distribution is significantly simplified in order to make the explanation easier to understand. In Fig. 5(a) and (b), the interacted magnetic flux between the transmitter and receiver pads does not vary even though the distance of misalignment increases from zero to D_{M}. As a result, the coupling between the primary and secondary coils will not decrease dramatically. With regard to the conventional planar square structure, a large portion of the interacted magnetic flux transforms into leakage magnetic flux when the misalignment distance increases from zero to D_M, as shown in Fig. 5(c) and (d). The decrease in interacted flux and increase in leakage flux result in a conspicuous drop of the coupling coefficient. Hence, the proposed structure offers better tolerance to misalignment than PSCS, which will be further verified in the subsequent sections.

III. OPTIMIZATION OF THE PROPOSED COUPLING STRUCTURE

Magnetic coupling and the capability of misalignment tolerance are highly associated with the dimensions of primary and secondary ferrites (SFs) and windings. In order to acquire optimal misalignment tolerance under the premise of preset minimum coupling coefficient, a series of simulation optimizations is conducted. The space constraints of the loosely coupled transformer (LCT) and PTD are given in Table I. It is important to note the dimensions of the primary and secondary coils are the maximum values of the superposed size of the ferrite and winding. For example, H_{sec} is 15 mm; therefore, the total height of the SF and SW ($H_{\text{SF}} + H_{\text{SW}}$, see Figs. 1 and 2) should be equal to or less than 15 mm.

The parameters, which are going to be optimized, along with their variation ranges, are given in Table II. These parameters are labeled in Figs. 1 and 2. The variation ranges of these parameters are mainly determined by the size constraints given in Table I. OSL_S is set to be equal to SL_{sec}, which is 300 mm in this study.

The optimization criteria determine the direction and purpose of an optimization. The optimization criterion of the proposed UCS is obtaining the strongest anti-misalignment capability

TABLE II
PARAMETERS TO BE OPTIMIZED

Parameter	Description	Variation range
H_P	Height of primary ferrite and winding	10 to 100 mm
W_{PW}	Width of primary winding	2 to 20 mm
OSL_{PW}	Outer side length of primary winding	50 to 150 mm
W_{PF}	Width of primary ferrite	2 to 20 mm
H_{SW}	Height of secondary winding	2 to 10 mm
H_{SF}	Height of secondary ferrite	2 to 10 mm
W_{SW}	Width of secondary winding	5 to 50 mm
W_{SF}	Width of secondary ferrite	10 to 100 mm

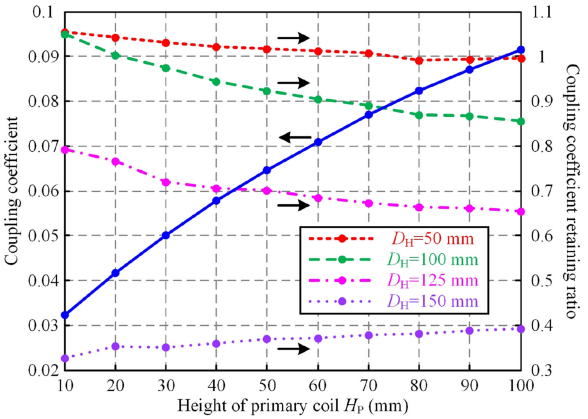

Fig. 6. Simulation results of coupling coefficient versus H_P and D_H.

while fulfilling the requirement of minimum coupling coefficient. Fig. 6 shows the simulation results of the coupling coefficient versus H_P and horizontal displacement D_H under the following condition:

$$\begin{cases} W_{\mathrm{PW}} = 2 \text{ mm} \\ \mathrm{OSL}_{\mathrm{PW}} = 60 \text{ mm} \\ W_{\mathrm{PF}} = 20 \text{ mm} \\ H_{\mathrm{SW}} = 2 \text{ mm} \\ H_{\mathrm{SF}} = 6 \text{ mm} \\ W_{\mathrm{SW}} = 5 \text{ mm} \\ W_{\mathrm{SF}} = 50 \text{ mm}. \end{cases} \tag{1}$$

It is worth noting the clearance between the PW and primary ferrite (PF), which is employed for insulation, is set to be 0.1 mm throughout the simulation. With both accuracy and efficiency incorporated, the optimization step of H_P is set as 10 mm. The coupling coefficient retaining ratio (CCRR) is defined by (2), where k_{mis} and k_{ali} stand for the coupling coefficient corresponding to the misaligned and aligned cases, respectively

$$\mathrm{CCRR} = \frac{k_{\mathrm{mis}}}{k_{\mathrm{ali}}}. \tag{2}$$

The coupling coefficient increases with H_P. Moreover, the increase of H_P has little adverse impact on the capability of misalignment tolerance of the proposed structure. Therefore, H_P is set as 100 mm in later simulations. It is also important to

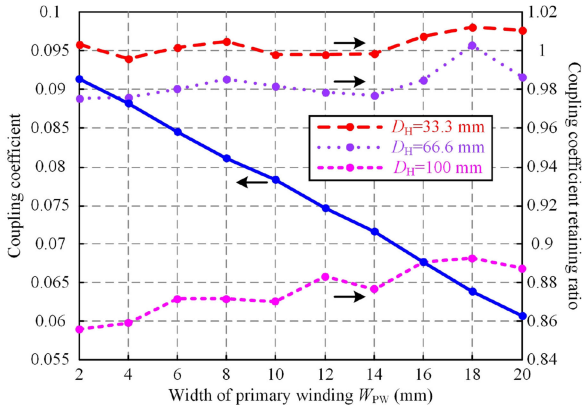

Fig. 7. Simulation results of coupling coefficient versus W_{PW} and D_H.

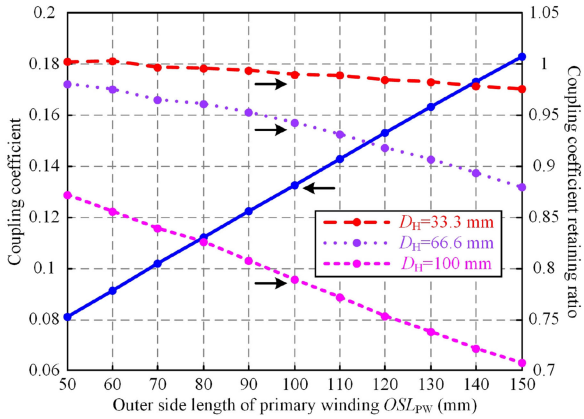

Fig. 8. Simulation results of coupling coefficient versus $\mathrm{OSL}_{\mathrm{PW}}$ and D_H.

note the marginal addition of the coupling coefficient becomes smaller when H_P is greater. With cost incorporated into the system design, H_P should not be extremely large. When H_P equals 100 mm, the CCRR stays as high as 0.856 at D_H of 100 mm. When D_H increases to 150 mm, the CCRR rapidly decreases to 0.393. It is difficult for an IPT system to maintain a rated output power in such a case. As a result, the maximum horizontal displacement is determined as 100 mm, one-third of the outer side length of the secondary coil.

Fig. 7 shows the profiles of coupling coefficient versus W_{PW} and D_H. W_{PW} is increased from 2 to 20 mm with a step of 2 mm, while the outer side length of the PF is set to be ($\mathrm{OSL}_{\mathrm{PW}} - 2 \times W_{\mathrm{PW}}$). The other simulation parameters are identical to those given in (1). The coupling coefficient decreases by 33.5%, from 0.0914 to 0.0608, when W_{PW} increases from 2 to 20 mm. However, the improvement of misalignment tolerance is inconspicuous. Consequently, W_{PW} should be as small as possible when $\mathrm{OSL}_{\mathrm{PW}}$ is determined.

What follows is the impact of $\mathrm{OSL}_{\mathrm{PW}}$ on coupling coefficient and misalignment tolerance. $\mathrm{OSL}_{\mathrm{PW}}$ is varied from 50 to 150 mm with an interval of 10 mm. The simulation results are depicted in Fig. 8. On one hand, the coupling coefficient increases, approximately linearly, with $\mathrm{OSL}_{\mathrm{PW}}$. On the other hand, the capability of misalignment tolerance deteriorates when $\mathrm{OSL}_{\mathrm{PW}}$ is increased. With the coupling coefficient and misalignment tol-

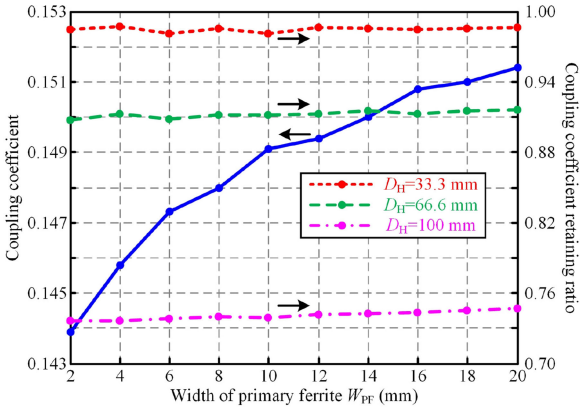

Fig. 9. Simulation results of coupling coefficient versus W_{PF} and D_H.

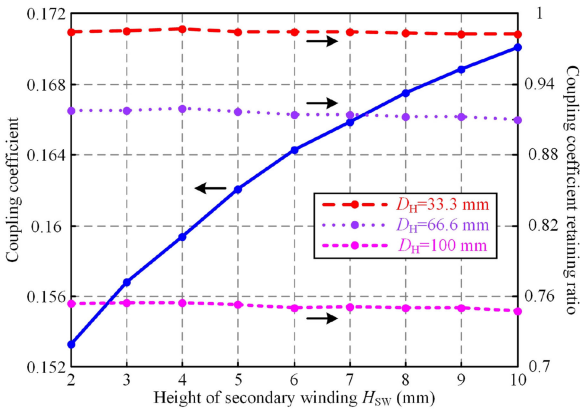

Fig. 10. Simulation results of coupling coefficient versus H_{SW} and D_H.

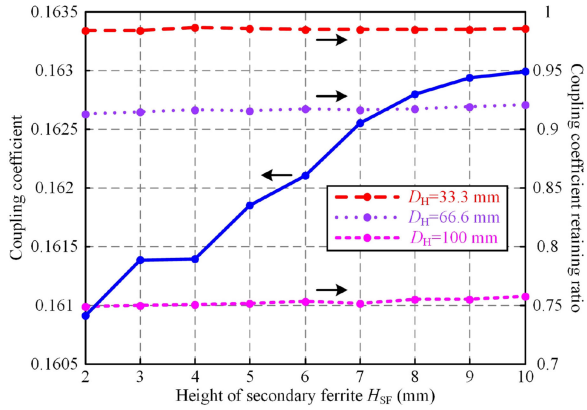

Fig. 11. Simulation results of coupling coefficient versus H_{SF} and D_H.

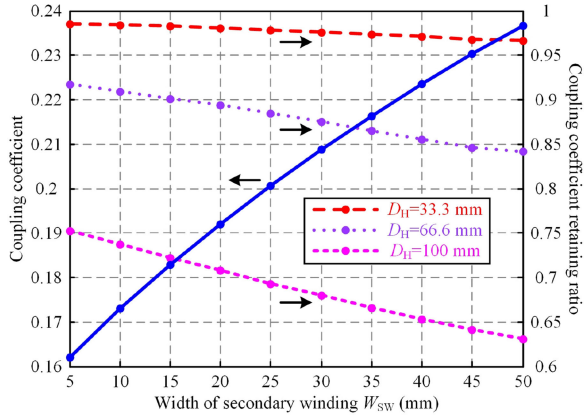

Fig. 12. Simulation results of coupling coefficient versus W_{SW} and D_H.

erance incorporated into the coil design, OSL_{PW} is determined as 120 mm.

Fig. 9 shows the simulation results of the coupling coefficient versus W_{PF} and D_H. With the increase of W_{PF}, both the coupling coefficient and misalignment tolerance are slightly improved. Nevertheless, the increase of W_{PF} leads to a significant rise in system weight and cost. As a result, a relatively small W_{PF} should be utilized in the proposed UCS. W_{PF} is set as 6 mm in the following simulations.

The influence of H_{SW} on the coupling coefficient and misalignment tolerance is investigated as well. Simulation results in Fig. 10 indicate that the increase of H_{SW} results in a higher coupling coefficient. Meanwhile, it has little adverse impact on misalignment tolerance. Taking the abovementioned two aspects into consideration, H_{SW} should be as large as possible to acquire a stronger magnetic coupling.

Fig. 11 shows simulation results of the coupling coefficient versus H_{SF} and D_H. H_{SW} is set to be 5 mm in the simulations. Although the coupling coefficient increases with H_{SF}, the increasing slope is quite small. The coupling coefficient only increases by 1.2% (from 0.161 to 0.163) when H_{SF}, as well as the volume, weight, and cost of the SF, increases by four times (from 2 to 10 mm). Moreover, the increase of H_{SF} makes little sense in improving the capability of misalignment tolerance. With the previous two points being incorporated into the coil design, H_{SF} should be as small as possible (under the premise of unsaturated SF) to reduce system volume, weight, and cost. It is finally determined as 5 mm because the ferrite strips with thinner height are not easily available in the market. Accordingly, H_{SW} is set to be 10 mm.

The impact of W_{SW} on coupling coefficient and misalignment tolerance is shown in Fig. 12. The coupling coefficient increases when W_{SW} is increased, but the capability of misalignment tolerance weakens. The most important motivation of this paper is constructing a high-misalignment magnetic coupling structure. The coupling coefficient is next in importance to misalignment tolerance. Hence, minimal W_{SW}, 5 mm, is selected in the proposed UCS.

As shown in Fig. 13, the coupling coefficient keeps increasing when W_{SF} increases from 10 to 100 mm. The deterioration of misalignment tolerance is hardly noticeable when W_{SF} is no more than 50 mm. When W_{SF} is greater than 50 mm, the decreasing slope of CCRR cannot be neglected. In order to achieve a higher coupling coefficient while maintaining sufficient misalignment tolerance, a tradeoff W_{SF} of 50 mm is selected.

Based on the optimization of the proposed UCS, several conclusions can be obtained. First, the larger the H_P, the higher the coupling coefficient is. Moreover, the misalignment tolerance is hardly affected by H_P. Thus, H_P should be as large as possible. Second, the increase of W_{PW} does little good to

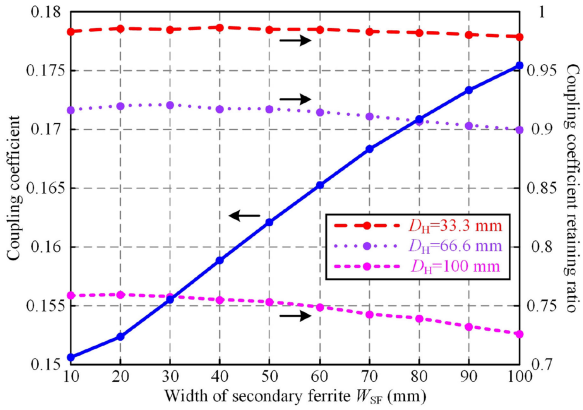

Fig. 13. Simulation results of coupling coefficient versus W_{SF} and D_H.

TABLE III
OPTIMAL VALUES OF THE GEOMETRY-RELATED PARAMETERS

Parameter	Optimal value
H_P	100 mm
W_{PW}	2 mm
OSL_{PW}	120 mm
W_{PF}	9 mm
H_{SW}	10 mm
H_{SF}	5 mm
W_{SW}	13 mm
W_{SF}	45 mm

the misalignment tolerance, but it does great harm to the coupling coefficient. Hence, W_{PW} should be as small as possible. Third, the increase of W_{PF} leads to a minor improvement in the coupling coefficient and misalignment tolerance, but it results in a significant rise in the system cost and weight. As a result, W_{PF} should be relatively small. Fourth, the misalignment tolerance is almost unaffected by H_{SW}. Nevertheless, the coupling coefficient increases with H_{SW}. Therefore, a bigger H_{SW} will be a better choice. Fifth, the improvement of misalignment tolerance by using thicker SF strips is less, but the increase of system volume, weight, and cost is remarkable. Consequently, under the premise of unsaturated SF, the minimum H_{SF} will be the optimal choice. The final derived value of each parameter is given in Table III. Some values are not exactly the same as those selected in the simulations due to practical constraints, including specifications of the ferrite strips, inductance of the coupling coils, etc.

The flowchart to achieve the optimized coupling coil is given in Fig. 14. For the sake of clarity, the parameters and variables are in bold. $D_{\text{H-max}}$ represents the maximum horizontal displacement, while CCRR_{min} stands for the minimum CCRR. The steps shown in Fig. 14 are much simpler than the optimization procedures mentioned above. The conclusions derived from this study, which are summarized in the last paragraph, can be exploited to directly determine the values of OSL_S, H_P, W_{PW}, W_{PF}, H_{SW}, and H_{SF} in later coil designs. We should follow the optimization criteria—misalignment tolerance first, coupling coefficient next—when determining the values of OSL_{PW}, W_{SW}, and W_{SF}.

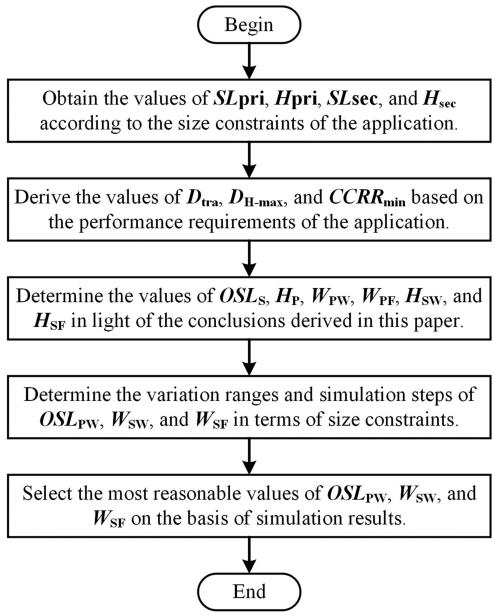

Fig. 14. Flowchart to achieve the optimized coupling coil.

IV. COMPARISON WITH THREE EXISTING COUPLING STRUCTURES

Planar circular and square coils and DD coupler are widely employed in the IPT field due to their simple structure, high-coupling coefficient, and good misalignment tolerance. The proposed structure is compared with these three coils in terms of magnetic coupling and anti-misalignment capability. Table IV gives more details on the comparison with respect to the single D winding (SDW), SW, PW, SF, PF, and PTD. The coupling coefficient under aligned condition (CC_{ali}) of the proposed structure is smaller than the other three structures, but this drawback is inevitable for achieving high misalignment tolerance. Moreover, system efficiency decreases much slower than the coupling coefficient. Although CC_{ali} of the proposed structure is much smaller than those of the other three structures, the system efficiency with the proposed structure is not.

The capability of the misalignment tolerance corresponding to the abovementioned four coupling structures is compared via Figs. 15–18. Fig. 15 depicts the CCRR of each coupling structure with respect to the *X*-direction displacement D_{H-X}. The CCRR of the proposed structure (CCRR_{pro}) stays highest when D_{H-X} is no more than 80 mm. When D_{H-X} increases to 90 or 100 mm, CCRR_{pro} takes the second place, a little lower than the DD coil. Generally speaking, the proposed structure and DD coupler possess similar capability in resisting *X*-direction displacement. When D_{H-X} equals 100 mm, one-third of the outer side length of the secondary coupling coil, CCRR_{pro} exceeds CCRR_{PS} (CCRR of planar square structure) and CCRR_{PC} (CCRR of planar circular structure) by 37.5% and 48.1%, respectively, indicating a much better *X*-direction misalignment tolerance.

Fig. 16 exhibits the CCRR of each coupling structure under different *Y*-direction displacements D_{H-Y}. CCRR_{pro}, CCRR_{PS}, and CCRR_{PC} in Fig. 16 are the same as those in Fig. 15 since

TABLE IV
COMPARISON BETWEEN THE CONVENTIONAL AND NEWLY PROPOSED COUPLING STRUCTURES

Coupling structure	Planar circular	Planar square	DD	Proposed
Overview	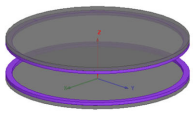	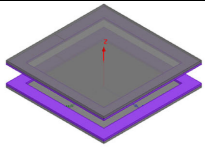	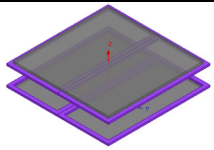	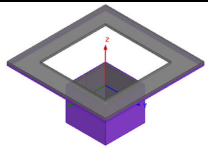
Enlarged coordinate system	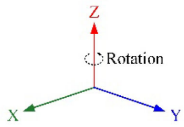	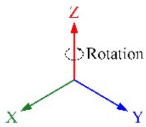	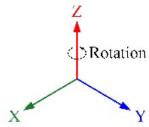	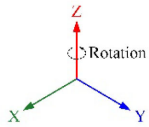
Coil size (mm)	Φ300/Φ280×5	[a]300/240×5	SDW: 300×150×5/280×130×5	SW: 300/290×5 PW: 120/116×100
Ferrite size (mm)	Φ300×5	300×300×5	280×280×5	SF: 300/200×5 PF: 116/106×100
PTD	50 mm	50 mm	50 mm	50 mm
CC_{ali}	0.326	0.440	0.440	0.155

[a]The size of square ring is expressed in following form: outer side length/inner side length×height.

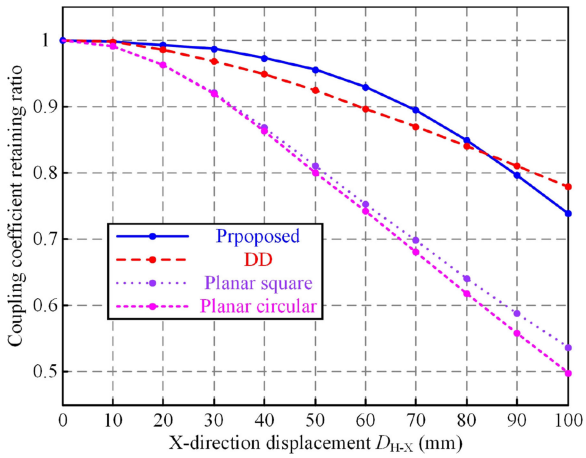

Fig. 15. Simulation results of CCRR versus *X*-direction displacement for four different coupling structures.

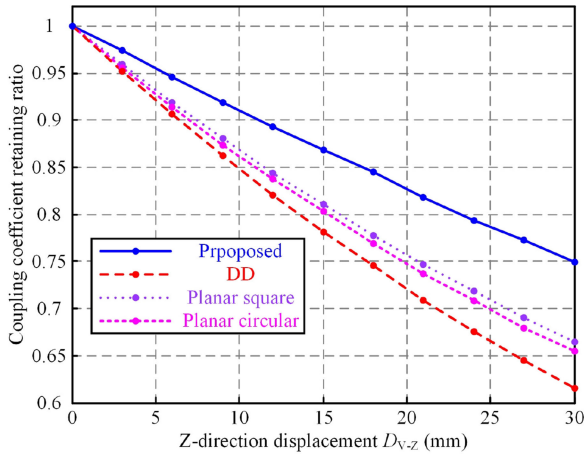

Fig. 17. Simulation results of CCRR versus *Z*-direction displacement for four different coupling structures.

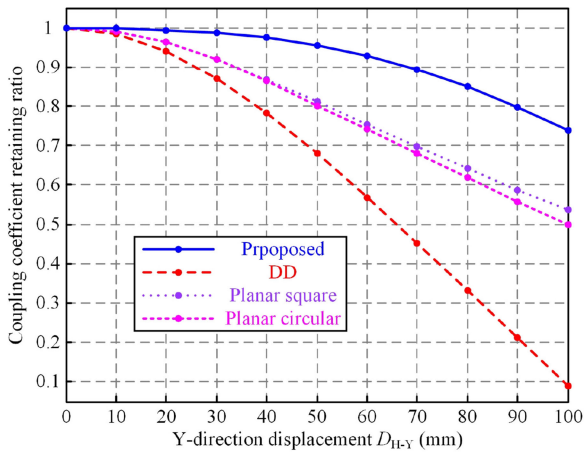

Fig. 16. Simulation results of CCRR versus *Y*-direction displacement for four different coupling structures.

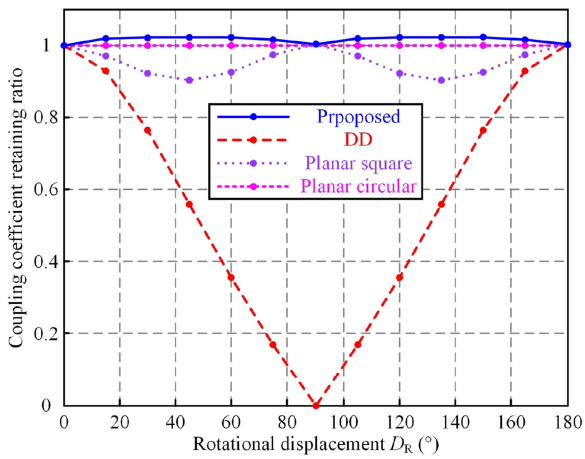

Fig. 18. Simulation results of CCRR versus rotational displacement for four different coupling structures.

the proposed structure, planar square, and circular coils are rotationally symmetric with respect to an angle of 90°. As regards the DD coupler, the capability of *Y*-direction misalignment tolerance gets much worse than that of the *X*-direction. It becomes the worst among these four structures. $\mathrm{CCRR_{pro}}$ remains highest when D_{H-Y} varies from 0 to 100 mm, implying optimal *Y*-direction misalignment tolerance. When D_{H-Y} equals 100 mm, $\mathrm{CCRR_{pro}}$ outstrips $\mathrm{CCRR_{PS}}$, $\mathrm{CCRR_{PC}}$, and $\mathrm{CCRR_{DD}}$ (CCRR of DD coupler) by 37.5%, 48.1%, and 712.1%, respectively.

Apart from a superior horizontal anti-misalignment capability, the proposed structure also offers better vertical misalignment tolerance than the other three structures, as shown in Fig. 17. When D_{V-Z} (*Z*-direction displacement) is 30 mm, three-fifth of the PTD, the CCRR of the four structures are in descending order of magnitude, 0.749, 0.6641, 0.6549, and 0.6151. $\mathrm{CCRR_{pro}}$ leads the other three structures by 12.8%, 14.4%, and 21.8%, respectively, at maximum vertical deviation. It is worth noting that the DD coupler is again the worst among these four structures.

Rotational deviation is inevitable in many applications; therefore, the capability of resisting rotational displacement is tested. The simulation results are shown in Fig. 18. When the receiver pad rotates around the *Z*-axis, the coupling coefficient of the planar circular coil remains constant, without any fluctuation. The coupling coefficient of the proposed structure is steady. It only increases by 2.1% when the rotation angle is 45°, where the biggest deviation of the coupling coefficient occurs. By contrast, the coupling coefficient of the planar square coil decreases by 9.7%, about 4.6 times as large as that of the proposed structure, at a rotation angle of 45°. With regard to the DD coupler, the coupling coefficient even decreases to zero when the receiver pad rotates 90° with respect to the transmitter pad.

Based on the preceding comprehensive analysis, the proposed magnetic coupling structure provides the best performance from the perspective of misalignment tolerance. The coupling coefficient can be maintained above 73.8% of CC_{ali} within the operation range ($D_{H-X} \leq 0.333 \times \mathrm{OSL}S$, $D_{H-Y} \leq 0.333 \times$ OSLS, $D_{V-Z} \leq 0.6 \times$ PTD, $0^\circ \leq D_{\mathrm{R}} \leq 360^\circ$). The output voltage ripple of an IPT system with proper compensation topology and a similar CCRR can be limited below 5% of the rated value.

Apart from the coupling coefficient and misalignment tolerance, the electromagnetic field (EMF) level is also very important to a magnetic coupling structure. The EMF level of the proposed structure is compared with the planar circular and square coils and DD coupler. The specifications of these four structures are the same as those given in Table IV. Fig. 19 shows the profiles of the EMF level in the plane which are parallel to the *X*–*Y* plane and located at the center of the primary and secondary coupling coils. These four structures are all symmetrical with respect to both *X* and *Y* axes. Therefore, only the region located in the first quadrant is considered. For the sake of fairness, the excitation current and inductance are set to be identical.

Fig. 19 shows that the DD structure provides the strongest magnetic flux intensity inside the coil and weakest outside the coil. From the perspectives of power transfer and human safety, the DD structure offers the optimum magnetic flux distribution. In addition to the DD structure, the other three structures have a similar magnetic flux distribution. The magnetic flux intensities inside and outside the coils are at an order of magnitude of 10^{-5} and 10^{-7}, respectively. Compared to the planar circular and square coils, the magnetic flux distribution of the proposed structure does not get worse.

V. Compensation Topology and Experiment Verification

The S/SP compensation topology proposed by Chen *et al.* has been deeply analyzed and widely employed [4]–[6]. Both theoretical analysis and practical experiment have demonstrated that S/SP topology possesses stronger anti-misalignment capability than primary series, secondary parallel topology. Besides, the S/SP topology provides the characteristic of load-independent output voltage when the system is operated under designed coupling coefficient. Moreover, the S/SP topology only needs three compensation capacitors. This makes great sense in improving PTE and power density since the equivalent series resistance, volume, and mass of a capacitor are generally much smaller than those of an inductor.

This paper selects the S/SP topology to verify the output voltage stability versus horizontal, vertical, and angular displacements. Fig. 20 shows the circuit diagram of the S/SP compensated IPT system that can be approximately divided into three parts—inverter, compensation capacitors and coupling coils, and rectifier and filter. The inverter is composed of a dc (direct current) voltage source U_{in} and four semiconductor switches Q_1–Q_4. The four switches constitute a full-bridge inverter, through which the input dc component is converted into high-frequency ac (alternating current) component. C_1, C_2, and C_3 are three compensation capacitors. L_P and L_S are, respectively, the primary and secondary self-inductances of the LCT, while *k* is the coupling coefficient. The high-frequency ac current flowing through the primary coupling coil generates high-frequency alternating magnetic field. The secondary coupling coil is located in the magnetic field and induces high-frequency ac voltage, which is subsequently converted to dc voltage by the rectifier and filter. D_1–D_4 are four Schottky diodes. They make up a full-wave uncontrolled rectifier. L_F and C_F are the filtering inductor and capacitor, respectively, and R_L is the resistive load.

The tuning method of compensation capacitances are given as follows:

$$\begin{cases} C_1 = 1/\left[\omega_0^2\left(1-k_d\right)L_P\right] \\ C_2 = 1/\left[\omega_0^2\left(1-k_d\right)L_S\right] \\ C_3 = 1/\left(\omega_0^2 k_d L_S\right) \end{cases} \tag{3}$$

where ω_0 is the system operation angular frequency and k_d is the designed coupling coefficient. It is very important to note that k_d can be either inside or outside the range of $[k_{\min}, k_{\max}]$. $k_{\min}$ is the minimum coupling coefficient which corresponds to the maximum displacement. $k_{\max}$ is the maximum coupling coefficient, which arises in the aligned case.

The parameters employed in the prototype are listed in Table V. Three compensation capacitors, C_1, C_2, and C_3, are

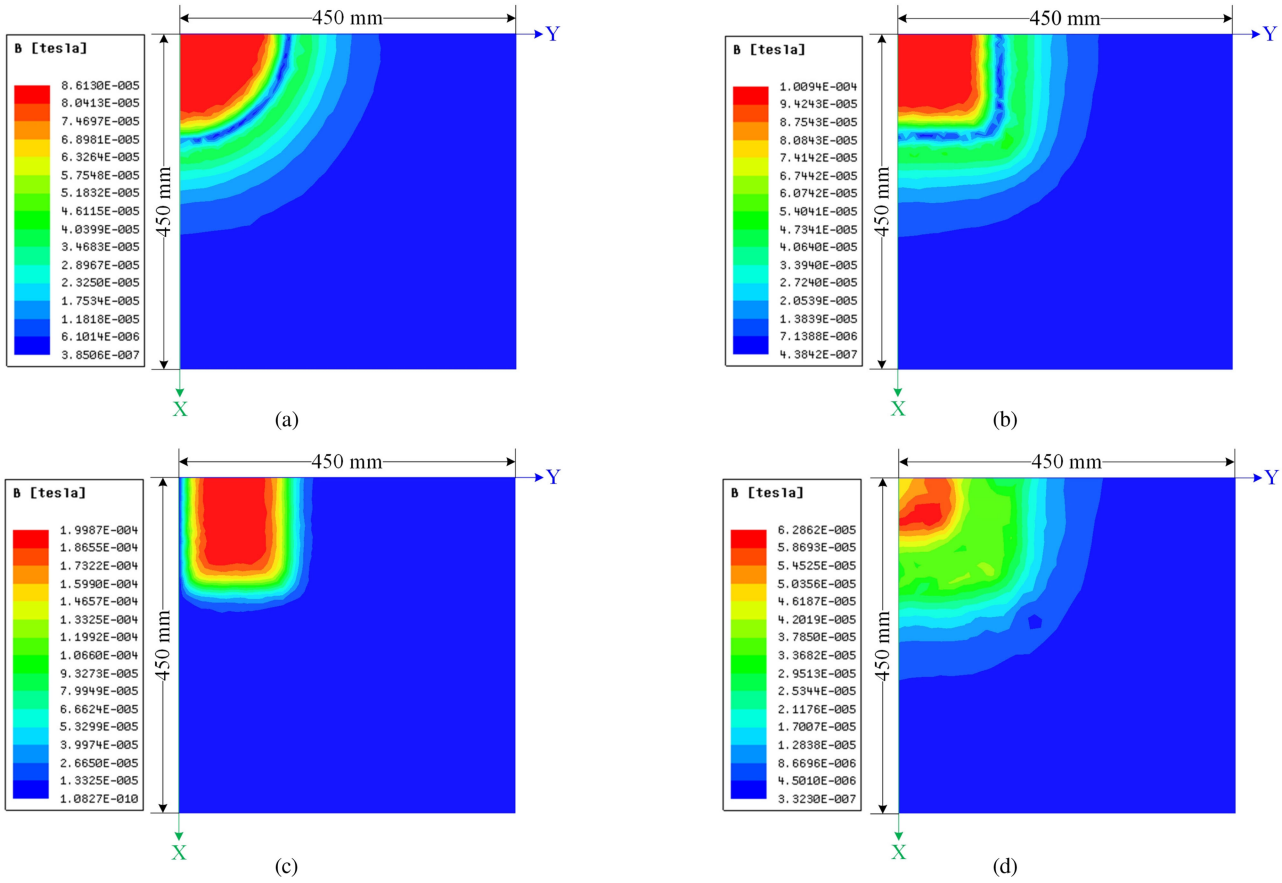

Fig. 19. Profiles of EMF level. (a) Planar circular structure. (b) Planar square structure. (c) DD structure. (d) Proposed structure.

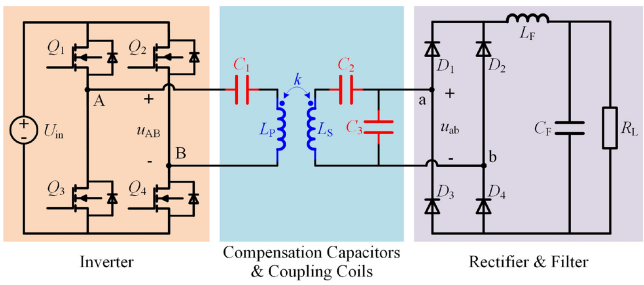

Fig. 20. Circuit diagram of the S/SP compensated IPT system.

TABLE V
PARAMETERS EMPLOYED IN THE PROPOSED PROTOTYPE

Parameter	Value/Type
Q_1~Q_4	SPW35N60CFD
L_P	135.5 μH
L_S	136.3 μH
k_{max}	0.1733
k_{min}	0.1288
C_1	37.6 nF
C_2	37.4 nF
C_3	82.4 nF
D_1~D_4	MBR30200PT
R_L	80 Ω

tuned at a coupling factor of 0.314 ($k_d = 0.314$). The validity of choosing such a k_d is verified by Pspice simulation. The simulation circuit is shown in Fig. 21(a) and the simulation results are shown in Fig. 21(b). The inverter in Fig. 20 is replaced by a high-frequency ac voltage source U_{AB} in terms of fundamental harmonic approximation method [23]. The rectifier and filter in Fig. 20 is substituted with its equivalent resistance R_E [24]. Fig. 21(b) indicates a nearly equal $u_{ab\text{-}k\min}$ and $u_{ab\text{-}k\max}$. This means the selected k_d is approximately the optimal value which will result in the lowest output voltage ripple factor (OVRF) when the coupling coefficient varies from k_{min} to k_{max}. The definition of OVRF is given by (4), where $U_{O\text{-max}}$ and $U_{O\text{-min}}$ represent the maximum and minimum output voltages, respectively. The OVRF is as low as 1.41% in the simulation

$$\text{OVRF} = \frac{U_{O-\max} - U_{O-\min}}{U_{O-\max} + U_{O-\min}}. \tag{4}$$

The photograph of the prototype is shown in Fig. 22(a). It is made up of five parts: dc voltage source, primary printed circuit board (PCB), proposed coupling structure, secondary PCB, and resistive load. They are numbered from 1 to 5 in order. The close-up view of the proposed coupling structure is given in Fig. 22(b). The side length of the transmitter pad is much smaller than that of the receiver pad.

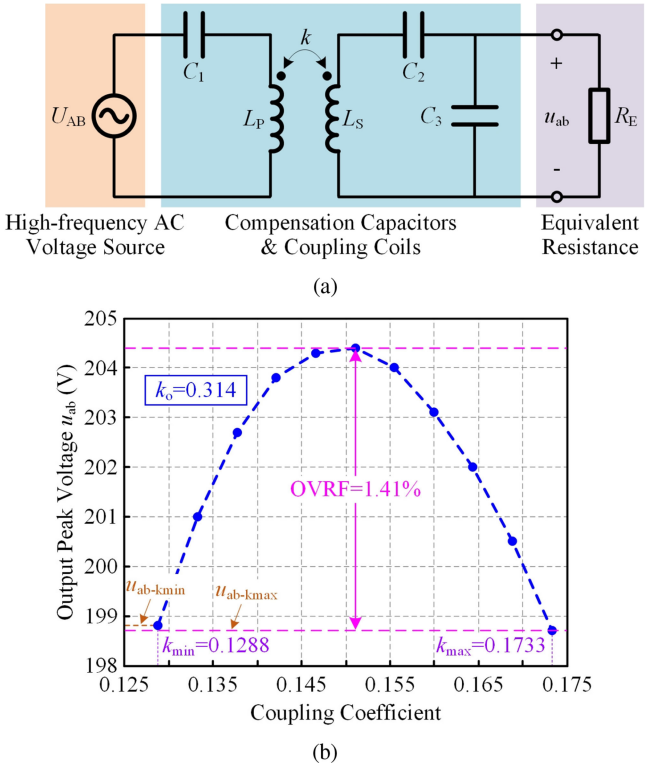

Fig. 21. Pspice simulation circuit and results. (a) Circuit. (b) Results.

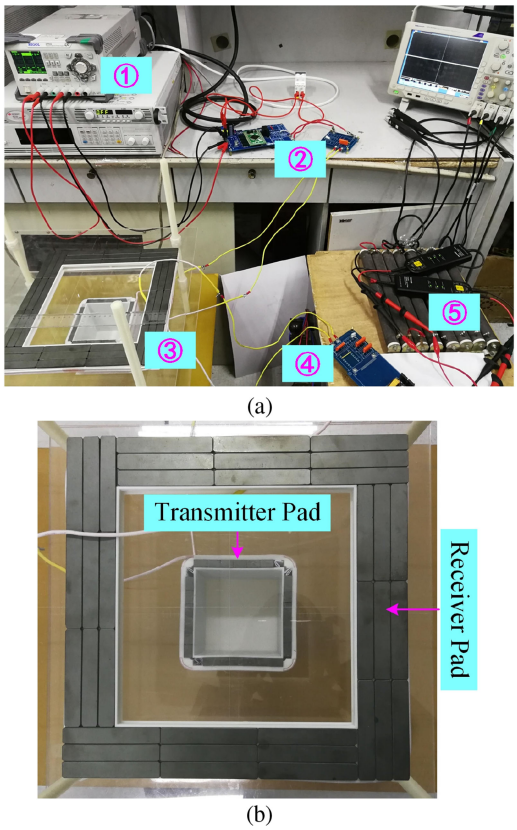

Fig. 22. Proposed experiment setup. (a) Photograph of the prototype. (b) Close-up view of the UCS.

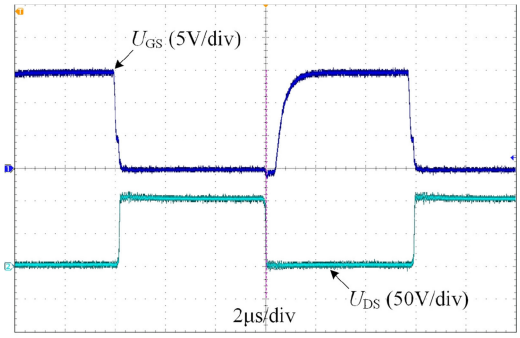

Fig. 23. Waveforms of U_{GS} and U_{DS} under aligned situation.

The waveforms of U_{GS} and U_{DS} are shown in Fig. 23. U_{GS} represents the voltage between the gate and source, while U_{DS} denotes the voltage between the drain and source. The waveforms are captured under aligned situation. U_{DS} has decreased to zero before the arising of the driving signal. Thus, zero voltage switching (ZVS) turn-ON is realized and the switching loss is significantly reduced. The duration of turn-OFF operation is very short, which further reduces the switching loss.

Fig. 24 presents the waveforms of the current and voltage stresses across each power stage when the coupling coefficient is 0.1733. The input and output powers are 213.2 and 200.7 W, respectively, indicating an end-to-end efficiency of 94.1%. Both the voltage stresses over the compensation capacitors and the current stresses through the coupling coils are quite small. Although the power of the proposed prototype is 200 W, it can be remarkably improved by employing higher input voltage, utilizing smaller resistive load, or manufacturing an LCT with smaller equivalent turns ratio $(L_P/L_S)^{0.5}$. Relatively low voltage and current stresses guarantee the feasibility of power improvement.

The experimental results of the output voltage and system efficiency with respect to horizontal, vertical, and angular displacements are shown in Figs. 25–27, respectively, according to which a maximum OVRF of 2.83% can be observed. Such a small ripple of voltage is accepted in most applications. In some special scenarios with strict OVRF requirements, a dc–dc converter can be series connected to the output. The highest system efficiency is 94.1%. It is achieved under the aligned case. The lowest system efficiency is 91.9%. It is obtained at a horizontal displacement of 10 cm. Even if a relatively large displacement takes place, the system efficiency can be kept at a high level. It is highly likely that the proposed structure will be employed in the IPT field in the near future.

Another IPT system utilizing the conventional planar square coils is fabricated. It is called comparative IPT system in this paper; therefore, it will not be mixed with the proposed IPT system, which is shown in Fig. 22. Both the primary and secondary coupling coils of the comparative system are the same as the secondary coupling coil of the proposed system. The compensation capacitances and coupling inductances of the comparative system, as well as the maximum and minimum coupling coefficients, are given in Table VI. C_1, C_2, and C_3 are tuned at a coupling coefficient of 0.443. The input dc voltage U_{in} is

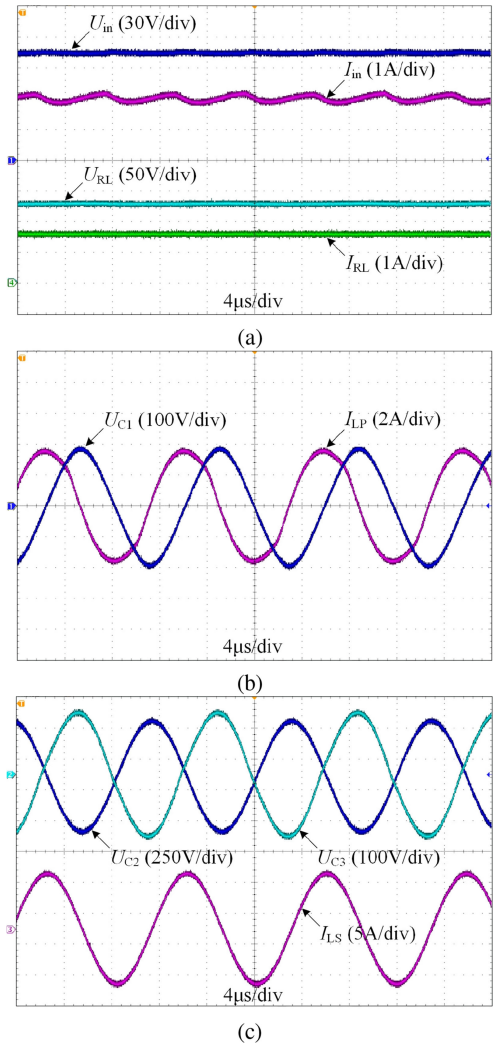

Fig. 24. Waveforms of current and voltage stresses across each power stage. (a) Input voltage and current and load voltage and current. (b) Voltage over C_1 and current through L_P. (c) Voltages over C_2 and C_3 and current through L_S.

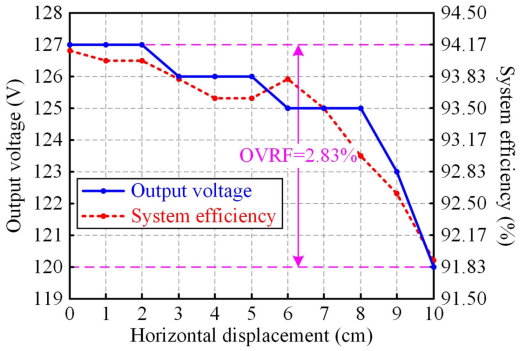

Fig. 25. Output voltage and overall efficiency of the proposed IPT system versus horizontal displacement.

increased to 125 V, aimed at obtaining an output power around 200 W. The other parameters utilized in the comparative system are identical to those employed in the proposed system.

Figs. 28–30 exhibit the experiment results of the comparative IPT system. On one hand, the overall efficiency of the

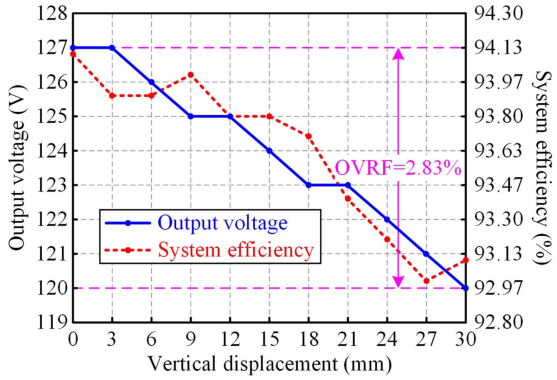

Fig. 26. Output voltage and overall efficiency of the proposed IPT system versus vertical displacement.

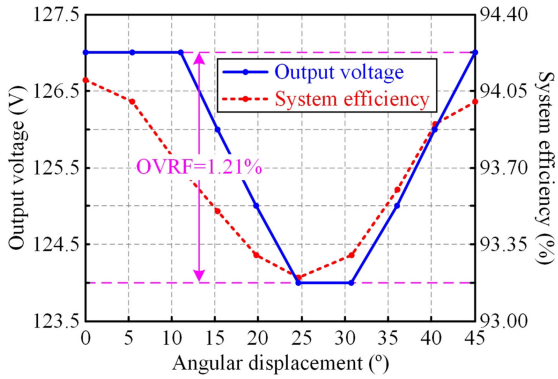

Fig. 27. Output voltage and overall efficiency of the proposed IPT system versus angular displacement.

TABLE VI
PARAMETERS EMPLOYED IN THE COMPARATIVE IPT SYSTEM USING PLANAR SQUARE COILS

Parameter	Value
L_P	136.2 μH
L_S	137.3 μH
k_{min}	0.1892
k_{max}	0.3236
C_1	46.6 nF
C_2	45.7 nF
C_3	57.1 nF

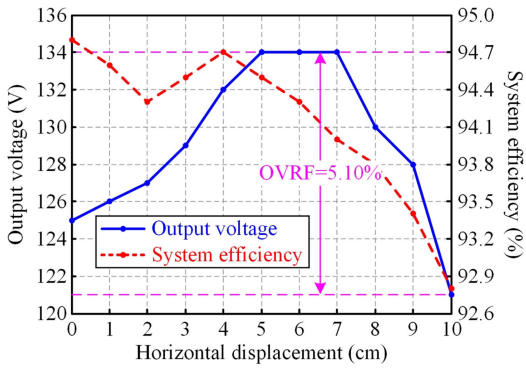

Fig. 28. Output voltage and overall efficiency of the comparative IPT system versus horizontal displacement.

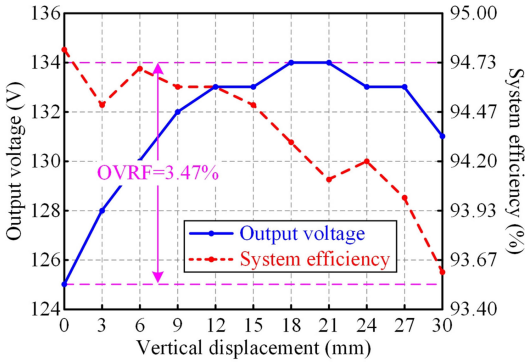

Fig. 29. Output voltage and overall efficiency of the comparative IPT system versus vertical displacement.

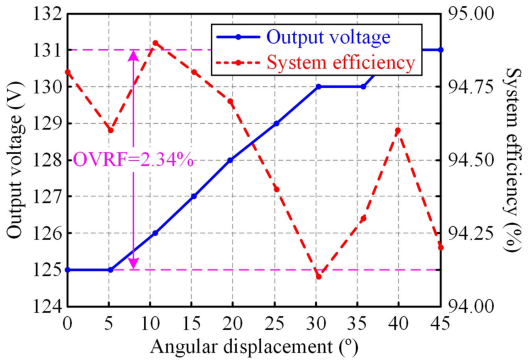

Fig. 30. Output voltage and overall efficiency of the comparative IPT system versus angular displacement.

comparative system is slightly higher than that of the proposed system due to a much bigger coupling coefficient. The highest PTE, 94.8%, is achieved when the primary and secondary coils are aligned. This maximum PTE is 0.7% higher than its counterpart displayed in Figs. 25–27. Although the coupling coefficient of the proposed system in an aligned case is 46.45% (1–0.1733/0.3236 ≈ 46.45%) lower than that of the comparative system, the PTE of the proposed system is only 0.74% (1–94.1%/94.8% ≈ 0.74%) lower than that of the comparative system. Experimental results have validated the claim that the PTE decreases much slower than the coupling coefficient. The PTEs of the comparative system in the following three cases, 1) with 10 cm *X*- or *Y*-direction displacement, 2) with 30 mm *Z*-direction displacement, and 3) with 25° angular displacement, are 92.8%, 93.6%, and 94.4%, respectively. They are 0.9%, 0.5%, and 1.2% higher than their respective counterparts shown in Figs. 25–27. On the other hand, the capability of misalignment tolerance of the comparative system is remarkably deteriorated when it is compared with the proposed system. Fig. 28 indicates an OVRF of 5.10% when the horizontal displacement varies from 0 to 10 cm. By contrast, the OVRF of the proposed system with an identical horizontal displacement is only 2.83% (see Fig. 25). In other words, the OVRF of the proposed system decreases by 44.5% when it is compared to the comparative system. In terms of Fig. 29, the maximum and minimum output voltages are 134 and 125 V, respectively, when the vertical displacement varies from 0 to 30 mm. The OVRF is subsequently calculated as 3.47%, which is 22.6% higher than its counterpart in Fig. 26. Experimental results in Fig. 30 illustrate that the comparative system is insensitive to angular misalignment because the OVRF is only 2.34% when the receiver pad rotates 45° with respect to the transmitter pad. In spite of this, the proposed system provides a stronger capability for angular misalignment tolerance. The OVRF of the proposed system is only 1.21%; 48.3% lower than that of the comparative system, when the angular displacement varies from 0° to 45°. In conclusion, the proposed system using UCS offers much stronger capability in resisting horizontal, vertical, and angular displacements than the system employing conventional planar square coils.

VI. Conclusion

This paper proposes a novel UCS, which can be utilized in high-misalignment situations. The concept of concentrated magnetic field is proposed. It is exploited to improve the capability of misalignment. The numerical optimization method is introduced, on the basis of which the optimal LCT is obtained. It is compared with the planar circular and square coils and DD coupler from the perspectives of magnetic coupling and anti-misalignment capability. Although the coupling factor of the proposed structure is lower than the other three structures, it performs much better in resisting horizontal, vertical, and angular displacements. Another important conclusion is that the DD coupler offers a stronger anti-misalignment capability only along the width of the coupler, while it performs worse in situations with other types of displacement. With the proposed unsymmetrical structure incorporated into the IPT system, a maximum OVRF of 2.83% can be acquired when $D_{\text{H-X}} \le 0.333 \times \text{OSL}_{\text{S}}$, $D_{\text{H-Y}} \le 0.333 \times \text{OSL}_{\text{S}}$, $D_{\text{V-Z}} \le 0.6 \times \text{PTD}$, $0° \le D_{\text{R}} \le 360°$.

References

[1] Chwei-Sen Wang, G. A. Covic, and O. H. Stielau, "Investigating an LCL load resonant inverter for inductive power transfer applications," *IEEE Trans. Power Electron.*, vol. 19, no. 4, pp. 995–1002, Jul. 2004.

[2] S. Wang, J. Chen, Z. Hu, C. Rong, and M. Liu, "Optimisation design for series–series dynamic WPT system maintaining stable transfer power," *IET Power Electron.*, vol. 10, no. 9, pp. 987–995, Jul. 2017.

[3] J. L. Villa, J. Sallan, J. F. Sanz Osorio, and A. Llombart, "High-misalignment tolerant compensation topology for ICPT systems," *IEEE Trans. Ind. Electron.*, vol. 59, no. 2, pp. 945–951, Feb. 2012.

[4] J. Hou, Q. Chen, X. Ren, S. C. Wong, and C. K. Tse, "Steady-state analysis of series/series-parallel compensated contactless resonant converter," in *Proc. IEEE 79th Veh. Technol. Conf. (Spring)*, Seoul, South Korea, 2014, pp. 1–5.

[5] J. Hou, Q. Chen, S. C. Wong, C. K. Tse, and X. Ruan, "Analysis and control of series/series-parallel compensated resonant converter for contactless power transfer," *IEEE J. Emerg. Sel. Topics Power Electron.*, vol. 3, no. 1, pp. 124–136, Mar. 2015.

[6] J. Hou, Q. Chen, X. Ren, X. Ruan, S. C. Wong, and C. K. Tse, "Precise characteristics analysis of series/series-parallel compensated contactless resonant converter," *IEEE J. Emerg. Sel. Topics Power Electron.*, vol. 3, no. 1, pp. 101–110, Mar. 2015.

[7] J. Zhao, T. Cai, S. Duan, H. Feng, C. Chen, and X. Zhang, "A general design method of primary compensation network for dynamic WPT system maintaining stable transmission power," *IEEE Trans. Power Electron.*, vol. 31, no. 12, pp. 8343–8358, Dec. 2016.

[8] H. Feng, T. Cai, S. Duan, J. Zhao, X. Zhang, and C. Chen, "An LCC-compensated resonant converter optimized for robust reaction to large coupling variation in dynamic wireless power transfer," *IEEE Trans. Ind. Electron.*, vol. 63, no. 10, pp. 6591–6601, Oct. 2016.

[9] Y. Wang, Y. Yao, X. Liu, and D. Xu, "S/CLC compensation topology analysis and circular coil design for wireless power transfer," *IEEE Trans. Transp. Electrific.*, vol. 3, no. 2, pp. 496–507, Jun. 2017.
[10] M. Budhia, J. T. Boys, G. A. Covic, and C. Y. Huang, "Development of a single-sided flux magnetic coupler for electric vehicle IPT charging systems," *IEEE Trans. Ind. Electron.*, vol. 60, no. 1, pp. 318–328, Jan. 2013.
[11] G. Yang, S. Dong, C. Zhu, R. Lu, G. Wei, and K. Song, "Design of a high lateral misalignment tolerance magnetic coupler for wireless power transfer systems," in *Proc. IEEE PELS Workshop Emerg. Technol.: Wireless Power Transfer*, Chongqing, China, 2017, pp. 34–39.
[12] A. Zaheer, D. Kacprzak, and G. A. Covic, "A bipolar receiver pad in a lumped IPT system for electric vehicle charging applications," in *Proc. IEEE Energy Conver. Congr. Expo.*, Raleigh, NC, USA, 2012, pp. 283–290.
[13] K. Aditya, V. K. Sood, and S. S. Williamson, "Magnetic characterization of unsymmetrical coil pairs using Archimedean spirals for wider misalignment tolerance in IPT systems," *IEEE Trans. Transp. Electrific.*, vol. 3, no. 2, pp. 454–463, Jun. 2017.
[14] X. Dai, L. Li, X. Yu, Y. Li, and Y. Sun, "A novel multi-degree freedom power pickup mechanism for inductively coupled power transfer system," *IEEE Trans. Magn.*, vol. 53, no. 5, pp. 1–7, May 2017.
[15] R. Carta and R. Puers, "Wireless power and data transmission for robotic capsule endoscopes," in *Proc. 18th IEEE Symp. Commun. Veh. Technol. Benelux*, Ghent, Belgium, 2011, pp. 1–6.
[16] S. Y. Choi, J. Huh, W. Y. Lee, and C. T. Rim, "Asymmetric coil sets for wireless stationary EV chargers with large lateral tolerance by dominant field analysis," *IEEE Trans. Power Electron.*, vol. 29, no. 12, pp. 6406–6420, Dec. 2014.
[17] N. Keeling, G. A. Covic, F. Hao, L. George, and J. T. Boys, "Variable tuning in LCL compensated contactless power transfer pickups," in *Proc. IEEE Energy Convers. Congr. Expo.*, San Jose, CA, USA, 2009, pp. 1826–1832.
[18] E. S. Lee, B. H. Choi, D. T. Nguyen, G. C. Jang, and C. T. Rim, "Versatile LED drivers for various electronic ballasts by variable switched capacitor," *IEEE Trans. Power Electron.*, vol. 31, no. 2, pp. 1489–1502, Feb. 2016.
[19] E. S. Lee, B. G. Choi, J. S. Choi, D. T. Nguyen, and C. T. Rim, "Wide-range adaptive IPT using dipole-coils with a reflector by variable switched capacitance," *IEEE Trans. Power Electron.*, vol. 32, no. 10, pp. 8054–8070, Oct. 2017.
[20] K. Fotopoulou and B. W. Flynn, "Wireless power transfer in loosely coupled links: Coil misalignment model," *IEEE Trans. Magn.*, vol. 47, no. 2, pp. 416–430, Feb. 2011.
[21] B. W. Flynn and K. Fotopoulou, "Rectifying loose coils: Wireless power transfer in loosely coupled inductive links with lateral and angular misalignment," *IEEE Microw. Mag.*, vol. 14, no. 2, pp. 48–54, Mar./Apr. 2013.
[22] J. P. K. Sampath, A. Alphones, and D. M. Vilathgamuwa, "Figure of merit for the optimization of wireless power transfer system against misalignment tolerance," *IEEE Trans. Power Electron.*, vol. 32, no. 6, pp. 4359–4369, Jun. 2017.
[23] Y. Wang, Y. Yao, X. Liu, D. Xu, and L. Cai, "An LC/S compensation topology and coil design technique for wireless power transfer," *IEEE Trans. Power Electron.*, vol. 33, no. 3, pp. 2007–2025, Mar. 2018.
[24] R. L. Steigerwald, "A comparison of half-bridge resonant converter topologies," *IEEE Trans. Power Electron.*, vol. 3, no. 2, pp. 174–182, Apr. 1988.

Yousu Yao (S'18) was born in Huai'an, Jiangsu, China, in 1991. He received the B.S. degree in electrical engineering from the Harbin Institute of Technology, Harbin, China, in 2014, where he is working toward the Ph.D. degree.

His research interests include inductive power transfer, magnetic coupling structure design, and wireless power and data transmission.

Dr. Yao was a recipient of the Best Paper Award for the year 2017 in the IEEE Transportation Electrification Conference and Expo, Asia-Pacific.

Yijie Wang (S'09–M'15–SM'15) was born in Heilongjiang, China, in 1982. He received the B.S., M.S., and Ph.D. degrees in electrical engineering from the Harbin Institute of Technology, Harbin, China, in 2005, 2007, and 2012, respectively.

He was a Lecturer with the Department of Electrical and Electronics Engineering, Harbin Institute of Technology, from 2012 to 2014. Since 2015, he has been an Associate Professor with the Department of Electrical and Electronics Engineering, Harbin Institute of Technology. His research interests include dc–dc converters, soft-switching power converters, power factor correction circuits, digital control electronic ballasts, and LED lighting systems.

Dr. Wang is an Associate Editor of IEEE TRANSACTIONS ON INDUSTRIAL ELECTRONICS, IEEE ACCESS, *IET Power Electronics*, and *Journal of Power Electronics*.

Xiaosheng Liu (M'14) was born in Qiqihar, Heilongjiang, China, in 1966. He received the B.S. and M.S. degrees in electrical engineering in 1988 and 1993, respectively, and the Ph.D. degree in mechatronics engineering in 1999, all from the Harbin Institute of Technology, Harbin, China.

Since 2006, he has been a Professor with the Department of Electrical Engineering, Harbin Institute of Technology. His research interests include power line communication and its routing methods, communication networks and control technology, and information and communication of smart grids.

Yu Pei was born in Kangping, Liaoning, China, in 1995. He received the B.S. degree in electrical engineering from the Harbin Institute of Technology, Harbin, China, in 2017, where he is working toward the M.S. degree in electrical engineering.

His research interests include wireless power transfer, magnetic coupling structure design, and closed-loop control.

Dianguo Xu (M'97–SM'12–F'17) received the B.S. degree in control engineering in 1982, and the M.S. and Ph.D. degrees in electrical engineering from the Harbin Institute of Technology (HIT), Harbin, China, in 1984 and 1989, respectively, all from the Harbin Institute of Technology (HIT), Harbin, China.

In 1984, he joined the Department of Electrical Engineering, HIT as an Assistant Professor. Since 1994, he has been a Professor with the Department of Electrical Engineering, HIT. From 2000 to 2010, he was the Dean of School of Electrical Engineering and Automation, HIT. He is now the Vice President of HIT. His research interests include renewable energy generation technology, power quality mitigation, sensorless vector controlled motor drives, and high performance permanent magnet synchronous motor servo system. He has authored over 600 technical papers.

Dr. Xu is a Fellow of IEEE, an Associate Editor of IEEE TRANSACTIONS ON INDUSTRIAL ELECTRONICS, IEEE TRANSACTIONS ON POWER ELECTRONICS, and IEEE JOURNAL OF EMERGING AND SELECTED TOPICS IN POWER ELECTRONICS. He serves as a Chairman of IEEE Harbin Section.